polysaccharides

MDPI

Article

Solute Energetics in Aqueous Xanthan Gum Solutions: What Can Be Learned from a Fluorescent Probe?

Mark P. Heitz [1,*], Emmanuel M. Nsengiyumva [1,2] and Paschalis Alexandridis [2]

[1] Department of Chemistry and Biochemistry, The State University of New York (SUNY) Brockport, Brockport, NY 14420-2971, USA; ensengiy@buffalo.edu
[2] Department of Chemical and Biological Engineering, University at Buffalo, The State University of New York (SUNY), Buffalo, NY 14260-4200, USA; palexand@buffalo.edu
* Correspondence: mheitz@brockport.edu

Abstract: Xanthan gum (XG) is a well-known anionic polysaccharide that finds broad application in the food and petroleum industries because of its ability to enhance solution viscosity at low concentrations and moderate temperatures. The aim of this work was to use the solvation probe coumarin 153 (C153) to characterize changes in the xanthan gum (XG) solution microstructure as a function of XG concentration and temperature from the perspective of a dissolved solute molecule. We established the utility of C153 fluorescence to track solution changes for XG concentrations that span the transition region from a dilute to a semi-dilute solution, defined by the xanthan gum overlap concentration, C*~0.02 g/dL. The temperature was varied from 293 to 353 K to probe solution conditions wherein XG has been reported to undergo a structural change from helix to random coil conformation, the details of which are still under debate. While C153 fluorescence does not elucidate direct structural information, the emission response is a simple means by which changes in aqueous XG solution can be identified. C153 spectroscopy is observed to correlate with XG conformational changes, as reported in the literature.

Keywords: biopolymer; polysaccharide; polyelectrolyte; xanthan gum; fluorescence spectroscopy; absorbance spectroscopy; coumarin 153; fluorescence lifetime

check for updates

Citation: Heitz, M.P.; Nsengiyumva, E.M.; Alexandridis, P. Solute Energetics in Aqueous Xanthan Gum Solutions: What Can Be Learned from a Fluorescent Probe? *Polysaccharides* **2024**, *5*, 892–910. https://doi.org/10.3390/polysaccharides5040055

Academic Editor: Emiliano Bedini

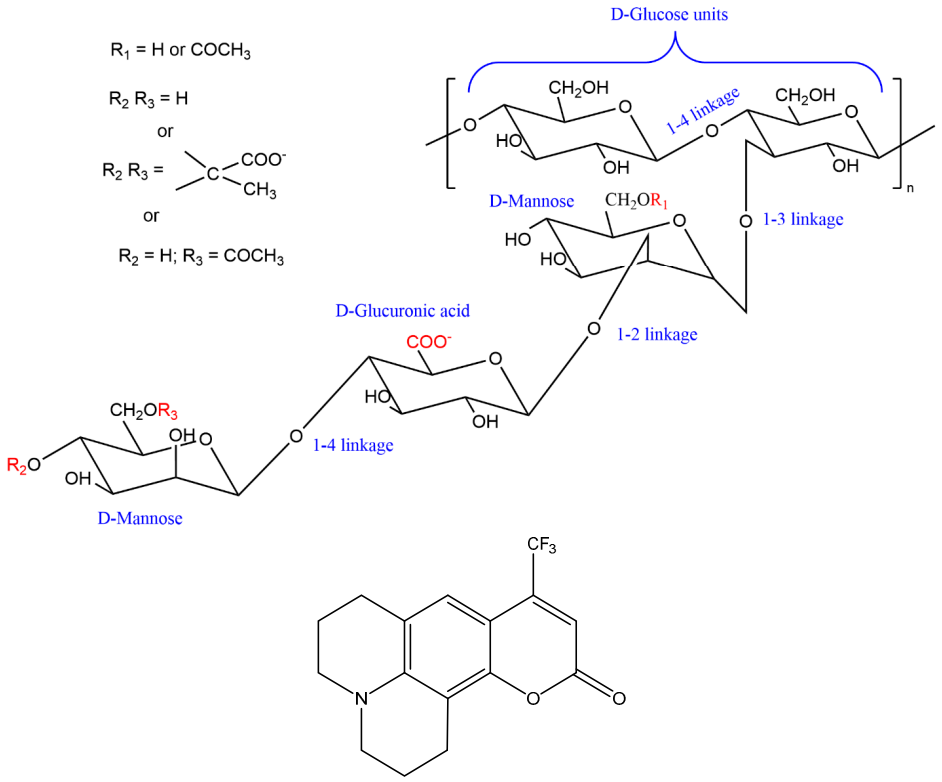
Received: 18 August 2024
Revised: 24 November 2024
Accepted: 13 December 2024
Published: 16 December 2024

Copyright: © 2024 by the authors. Licensee MDPI, Basel, Switzerland. This article is an open access article distributed under the terms and conditions of the Creative Commons Attribution (CC BY) license (https://creativecommons.org/licenses/by/4.0/).

1. Introduction

Biopolymers, including polysaccharides such as xanthan gum, chitin, pullulan, hyaluronic acid, carrageenan, glucans, guar gum, cellulose, and dextran, are renewable resources derived from plants, seaweeds, animals, and bacterial fermentation [1]. These polymers have a diversity of chemical structures and thus properties that make them good candidate materials for sustainable applications because they demonstrate biodegradability, biocompatibility, and bio-adhesion [2]. These materials are important to understand as they provide guidelines for the selection of complex fluids or rheology modifiers [3]. In the class of biopolymers, the anionic polysaccharide xanthan gum (XG, Scheme 1) is an environmentally friendly and water-soluble biopolymer. Excellent reviews that highlight the extensive utility of XG are available [2,4–8]. It has been approved by the United States Food and Drug Administration (FDA) since 1969 as a food additive. XG is among the most important commercially available and low-cost microbial polysaccharides. Because of its rheological and pseudoplastic properties, it is widely used as a thickener or emulsifier agent that finds many applications in food products [4], including salad dressing, ice cream, and yogurt [9]. Many diverse applications of XG are seen across various fields, including oil-field development [10], drug delivery [8], drag reduction [1], biomedical [11], pharmaceutical [12], agriculture [13], mining [6], battery [14], and environmental fields [5,7]. XG is attractive for a considerable range of applications as it is a well-known, nontoxic, biodegradable, biocompatible, and bio-adhesive polymer [15]. XG is produced by fermentation of *Xanthomonas campestris*, with a primary structure consisting of the trisaccharide

β-D-mannose-(1-4)-α-D-glucuronic acid-(1-2)-α-D-mannose linked to the O(3) position of every other glucose residue [16]. Pyruvic acid residues are linked through ketal bonds to roughly 50% of the terminal mannose residues [17]. These mannose residues also include acetate groups. Structural variability—the extent of pyruvate and acetate group substitution—is controlled by the culture and fermentation process conditions [18]. The degree of acetate and pyruvate inclusion influences the XG threshold temperature, where XG is reported to undergo an order/disorder transition from a helical conformation to a random coil conformation [19,20]. The XG backbone consists of both hydroxyls and carboxyls along with glycosidic oxygen atoms, all of which govern intermolecular hydrogen bonding [21]. XG molecular weights are reported to range between 1 and 20 × 10^6 g/mol [16] with an estimated average molecular weight of 2 × 10^6 g/mol [22]. The large molecular weight, coupled with intermolecular hydrogen bonding interactions, results in XG behaving as a pseudoplastic, and its viscosity increases with polymer concentration in water [23].



Scheme 1. Structures of xanthan gum and coumarin 153 (C153).

The secondary structure of XG exists in three forms: (i) native, single-stranded helix; (ii) double or triple helix, rigid structure; and (iii) disordered, flexible chains [24,25]. The structural details of the helical conformation remain controversial. The conformation transitions are influenced by temperature, pH, salt content, solvent quality, shear rate, and other environmental conditions [26]. The disordered conformation, or random coil, can be described as a broken or imperfect helix [9]. XG chains extend in non-saline aqueous media because of intra-chain electrostatic repulsion between charged groups on the side chains. In salt-free aqueous solutions, xanthan gum chains retain their high degree of rigidity with some degree of flexible conformation [16,27]. In the absence of ionic content, XG is surrounded by a cloud of counterions that exactly balances the charge on the chains, and its aqueous solution maintains charge neutrality [27]. Due to the charge balance in non-saline environments, the XG molecular configuration is sensitive to added salt ions in solution [28]. In the presence of salts (brine solution), XG assumes an ordered, helical conformation that is

more rigid and rod-like than the disordered conformation as a function of salt concentration and solution temperature [29,30]. Specifically, XG chains in the ordered conformation are much more rigid, with an estimated Kuhn segment length [31] (L_k) of 240 ± 40 nm in terms of the wormlike chain model compared to the disordered structure (L_k = 42 nm). The XG intrinsic persistence length is similar to that of the single helical structure of DNA (~50 nm) and the double helical structure (~120–148 nm) in salt solution [32]. The presence of salt in solution causes shielding of electrostatic repulsion between charged groups, making the XG macromolecules assume a more compact structure [33]. This decreases the polymer chain size and the number of interactions with the neighboring chains [16]. The degree to which a polymer molecule's conformation shrinks may be dependent on the stiffness of the polymer chain in solution [27].

Results from Rochefort et al. show that the ordered conformation of keltrol XG (~3.5 × 10^6 g/mol, 0.5 g/L) is attained at a salt concentration above 10^{-2} M NaCl, and no further salt effects should be noted [9]. Comparing the molecular weight of XG (3 to 5 × 10^5 g/mol, 3.1–6.4 mg/mL) in 5 mM and 100 mM NaCl, the molecular weight values are smaller at 5 mM, which indicates a partly unfolded structure in the low-ionic-strength solvent [31]. Brunchi and colleagues found that the intrinsic viscosity of XG (1.165 × 10^6 g/mol) increases with temperatures rising from 25 to 75 °C in salt-free solutions and in 10^{-5} and 10^{-2} M NaCl [26]. A low intrinsic viscosity indicates ordered conformation chains, while an increase in intrinsic viscosity suggests a disordered conformation. Rinaudo et al. estimated a persistence length for XG (~10^6 g/mol, 0.01 M NaCl) of 30 nm and 125 nm for the double helix structure after renaturation or cooling below 25 °C [24,34]. Philippova and colleagues reported a side-by-side association of xanthan double helices at 0.15 and 0.5 wt % in 0.64 M KCl (via FF-TEM, 1 × 10^6 g/mol, and 0.5–2 wt %) [35]. At a fixed ionic strength of 10 mM NaCl, the observed helix–coil transition occurs at high temperatures (near 50 °C) with reduced XG pyruvate levels, while reducing acetate content reduces the transition temperature [36]. Acetate content stabilizes the ordered conformation because of intramolecular attractive interactions, while pyruvate inhibits the formation of the ordered structure due to intermolecular electrostatic interactions [26].

While much attention has been given to XG solutions under a variety of experimental conditions such as pH, ionic strength, temperature, and shear rate, the XG conformational transition from helix to random coil in response to experimental stimuli is still a subject of interest as it is not fully understood. Moreover, most work has been conducted using direct solution probing by means of bulk physicochemical measures such as rheology, density, viscosity, and conductivity experiments. Various scattering techniques, including small- and wide-angle neutron scattering and x-ray scattering, have also been applied to examine XG structural organization. To the best of our knowledge, there is no report using optical emission spectroscopy, e.g., fluorescence emission spectroscopy, to probe and characterize XG solution characteristics at a microscopic level from the perspective of an extrinsic molecular probe. Fluorescent probes like BODIPY (4,4′-difluoro-4bora-3a,4a-diaza-s-indacene) and DASPMI (4-(4-(dimethylamino)styryl)-N-methyl-pyridinium iodide) have been used to monitor changes in fluorescence lifetime, which were related to changes in gellan gum solution viscosity [37]. Fluorescence spectroscopy provides a convenient, direct method for probing the microenvironment and has been used to track organizational changes that occur at the micro- and nanoscopic level in diverse media such as sol-to-gel transitions [37], aggregation in surfactant solutions [38], protein–ionic liquid interactions [39], and strand architecture of amyloid fiber formation [40]. For XG, the hydrophobic association with grafted C16 carbon chains was studied using pyrene and anilinonaphthalene sulfonate (ANS) to determine the modified XG change in hydrophobicity [41]. While it is important to understand the fundamental nature of XG-XG interactions under various solution compositions and conditions, the numerous chemical and engineering applications that use XG as an enhancement medium suggest that there is also value in examining solution behavior using indirect probing via a molecular

solute [15,21,42–48]. Thus, here we examine the steady-state and time-resolved fluorescence emission of coumarin 153 (C153) as an independent means of probing XG interactions, with the goal of assessing the solution microenvironment effects on a solute molecule. Simultaneously, the observed effects provide direct insight into XG solution changes. The data presented here augment our understanding of XG concentration and temperature effects from the unique perspective that an extrinsic fluorophore offers, helping to elucidate the medium modifier behavior in the XG/water system.

2. Materials and Methods

The food-grade xanthan gum used in this study is commercially available in a wide range of particle sizes, (CPKelco, Atlanta, GA, USA; material number: 10040281), with an estimated molecular weight of 2×10^6 g/mol and a polydispersity index ~2 [28,49]. The polymer was received in powder form and used without further purification or modification. The deionized water used was purified with a MilliQ system with a measured resistance of 18.2 MΩ cm. A 0.16 wt % xanthan gum stock solution was prepared by dispersing dried xanthan gum in deionized water. The stock solution was gently stirred for 24 h at 20 °C to obtain a fully hydrated solution that appeared translucent and was kept refrigerated at 4 °C to minimize bacterial growth. When solutions were diluted for measurement, they were equilibrated at room temperature for at least 1 h and were observed to be optically transparent. Appropriate volumes of the xanthan gum stock solution were pipetted into deionized water to prepare the desired xanthan gum solution concentrations.

Coumarin 153 (C153, Scheme 1) was purchased from Exciton (Lockbourne, OH, USA), stored under desiccation, and used as received. To prepare a sample for measurement, C153 was pipetted from a methanol stock solution, and the solvent was thoroughly evaporated using a gentle stream of dry ultrapure nitrogen prior to the addition of XG solution. The probe concentration was ~10 μM, and the resulting solution optical density (absorbance) was not more than 0.1 at the laser excitation wavelengths, 405 and 425 nm, as is typical to minimize inner filter effects [50,51]. Solutions were mixed by repeatedly inverting the cuvette to form a single-phase, transparent solution.

Steady-state absorbance was measured using a Perkin-Elmer Lambda 800 UV–vis spectrometer, with slit settings that provided 2 nm spectral resolution. Fluorescence excitation and emission spectra were recorded on a Horiba Scientific Fluorolog-3 fluorescence spectrometer (Horiba Scientific, Piscataway, NJ, USA) with a 2 nm resolution. A 450 W Xe arc lamp and a single-grating monochromator were used for excitation, while emission was measured through a double-subtractive grating monochromator for enhanced stray light rejection. Detection was performed using a Hamamatsu R928P PMT (Hamamatsu Photonics, Shizuoka, Japan). Calibration was performed daily using the Raman signal from deionized water with 350 nm excitation and observing Raman scatter at 397 nm, and the signal-to-noise ratio was always greater than 5000:1. A National Institute of Standards and Technology (NIST) calibration lamp was used to generate excitation and emission correction files for both intensity and wavelength instrument correction procedures. All spectra were further corrected by applying blank solvent subtractions to correct for sample response. Replicate data were combined to yield spectral uncertainties that were not larger than 100 cm^{-1} in all cases, and the intensity percent variation at the peak of emission was not more than 5%. To compute the normalized intensity for each spectrum, the entirety of each spectrum was ratioed to its absolute maximum intensity value.

Time-correlated single photon counting (TCSPC) fluorescence instrumentation (Tau-3 system, Horiba Scientific, Piscataway, NJ, USA) was used as previously described [52]. Intensity decays were measured with excitation by a 405 nm NanoLED (405-L) diode laser operated at a 1 MHz repetition rate. Excitation photons were vertically polarized prior to entering the sample chamber, and the subsequent emission was passed through a Glan-Thompson polarizer set at the "magic" angle (54.7°) for excited-state decay kinetics, spectrally resolved through the Fluorolog-3 emission monochromator, and detected with an IBH TBX 850 detector (Horiba Ltd., Kyoto, Japan). Data were collected to 10,000 counts

in the peak channel in accord with Poisson statistics for photon counting measurements. Instrument response was determined using a glycogen scattering solution, and typical values were ~180 ps. The instrument time calibration was 7.1 ps per channel. Decay data were measured at the peak of the steady-state emission, with a 5 nm bandpass unless otherwise stated. For TCSPC analysis, the intensity decays were evaluated using DAS6 (version 6.6) decay analysis software. We estimated that the effective time resolution was ~50 ps following a least-squares reconvolution fitting of the intensity decay. The quality of fits to a sum-of-exponentials model was assessed using reduced chi-squared values, and a fit was judged acceptable if $\chi_r{}^2 < 1.2$. When the data appeared to need multiple time constants, we allowed the inclusion of an additional time constant only if there was at least a 10% improvement (decrease) in $\chi_r{}^2$, along with a discernable improvement in fitting residuals with a concomitant improvement in the autocorrelation of the residuals. In this way, the estimated uncertainty in fitted decay time constants was not more than $\pm$0.08 ns.

An independent set of time-resolved 2D fluorescence measurements was performed using a Ti:sapphire streak camera spectrometer (HAMAMATSU PHOTONICS, Hamamatsu City, Japan) to check for solute dynamics that exceed the resolution lower limit of the TCSPC instrument. Fluorophore excitation was achieved using a Spectra-Physics Mai Tai femtosecond oscillator (Spectra-Physics, Milpitas, CA, USA) producing 2.95 W average power at 850 nm with a repetition rate of 80 MHz and pulse width of ~80 fs FWHM. The beam diameter was approximately 100 µm. The fundamental beam fed a GWU (Erftstadt, Germany) Ultrafast Harmonic Generator (UHG) unit that housed a Bragg cell pulse selector and BBO crystal for frequency doubling. The 80 MHz pulse train was first reduced to 80 kHz with the Bragg cell and then the frequency was doubled to 425 nm for sample excitation, with an average doubled power of ~200 µW. The various table optics used here were purchased from Newport Corporation (North Logan, UT, USA). Prior to entering the sample, the beam was passed through a half-wave plate followed by a Glan-Laser polarizer and was then focused on the sample using a 100 mm focal length 25.4 mm diameter plano-convex lens. Emission from the sample was collected, collimated, and passed through a matching Glan-Laser polarizer to set emission polarization at the magic angle (54.7°) with respect to excitation. A polarization scrambler and focusing lens steered the emission into a SpectroPro 150 mm spectrograph (Teledyne Princeton Instruments, Trenton, NJ, USA). The output of the spectrograph was finally focused on the universal streak camera, model C10910 with model M10912 (Hamamatsu, Bridgewater, NJ, USA). Spectrograph and streak slits were set at 50 µm and 30 µm to maximize spectral and time resolution, respectively. Analysis code was written in-house using Igor Pro 9 (WaveMetrics, Portland, OR, USA).

3. Results and Discussion

3.1. Steady-State Spectroscopy

C153 is known for its sensitive spectral response to the surrounding microenvironment, resulting from the ~8 D change in the dipole moment upon excitation to the electronic excited state [53,54]. The polar nature of the C153 ground state, 6.55 D [55], and excited state, 14.5 D [56], makes C153 a reasonable choice to study the XG/water interactions. The fluorinated moiety of C153 enhances the ability of this polar molecule to respond to ensemble microenvironments that are less polar while simultaneously solubilizing in polar microdomains. Its solvatochromatic response is well documented [57,58]. Moreover, the presence of the fluorine and oxygen atoms within the molecular structure also favors hydrogen bonding interactions, further enhancing observed spectral shifts in response to solution properties [59]. In typical polar solvents such as acetonitrile or methanol, C153 is strongly fluorescent and exhibits larger quantum yields [58,60,61] compared to that observed in water, where the C153 emission is redshifted and significantly quenched. Temperature also influences the C153 spectral response. In chloropropane, a decrease in molar absorptivity and a blueshift in the absorbance maximum is observed with increasing temperature, with similar behavior noted for the emission [62,63]. Through these spectral response features, C153 is expected to differentiate between XG domains and water domains

insofar as XG forms a solvated structure. Steady-state spectroscopy alone is unlikely to clearly distinguish between specific structural motifs such as conformational change or XG-XG aggregation because either situation may modulate the micro- or nanoheterogenous solution structure.

3.1.1. XG Concentration Effect

The concentration dependence of XG ordering in aqueous solution has been shown through scattering studies [64] and physical property measurements [28,65–67]. For example, increasing the XG concentration from 0.4 to 2.0% increased viscoelastic stability, viscoelastic moduli, and widened linear viscoelastic regions [68]. XG reduced viscosity increases with dilution, indicating the characteristics of polyelectrolyte behavior due to electrostatic repulsion interactions [69]. Milas and coworkers used small-angle neutron scattering to suggest an XG conformation transition that favors a helical (ordered) conformation at decreased temperature (298 K) and with decreasing XG concentration, interpreting the ordered-to-disordered conformation [64]. It is also plausible to consider that interaction mechanisms may include concentration effects due to molecular aggregation and entwined interactions but at high concentrations, even up to 1 g/dL, as reported by Papagiannopoulos and coworkers [32,70]. We note that this effect was only observed at concentrations in semi-dilute or more concentrated solutions, well beyond our highest solution concentrations. Thus, XG aggregation is unlikely when working in a dilute solution and at best may only begin to manifest in a semi-dilute solution, relative to C*. However, the detailed molecular underpinnings of the XG concentration dependence are not yet fully explained, and spectroscopy offers an additional perspective. Examples of the C153 spectral response to XG concentration are presented in Figure 1. The upper panels of Figure 1 show the absolute emission intensity changes for XG concentrations at 303 K and 343 K. We expect the C153 quantum yield to be sensitive to XG solution microstructure, depending on the water environment sensed, as water quenches C153 emission, and the observed intensity variation confirms this response. The spectral response further showed that at higher temperatures (Figure 1, upper right panel) the intensity maximum at each concentration consistently increased by at least threefold at 343 K compared to 303 K for all XG concentrations measured. We note that some care must be used with the interpretation of absolute intensity changes since small variations in sample preparation may occur, such as pipetting volumes of stock solution, which could result in small but potentially detectable variations in the measured absolute intensity. Nonetheless, the magnitude changes are very much larger than what might be caused by less accurate pipetting, and although we cannot be completely quantitative in the absence of measured quantum yields, the gross trends observed here are consistent and demonstrate the C153 fluorescence sensitivity to concentration and temperature effects. Given this, we prefer to use a more reliable evaluation metric and, therefore, view the spectral response using a normalized intensity metric, as shown in the lower panels of Figure 1. Several features of these data emerge. First, at 303 K the spectra reveal only a slight variation in the overall emission as [XG] increases, though from the spectral plots, the magnitude is difficult to discern. While peak position suggests only a slight variation, the half-maximum intensities show an XG-concentration-dependent spectral shift and shape change, where the longer wavelength "red" edge emission remains constant to within uncertainty, and the "blue" edge emission shifts to higher energy, as indicated by the arrow. In contrast, at higher temperatures, we observe a negligible effect on wavelength and spectral shape. Thus, at higher temperatures, the intensity variation is the key parameter that shows the C153 response to concentration changes, and the lack of spectral shift indicates a more homogeneous chemical environment about C153 at 343 K compared to 303 K.

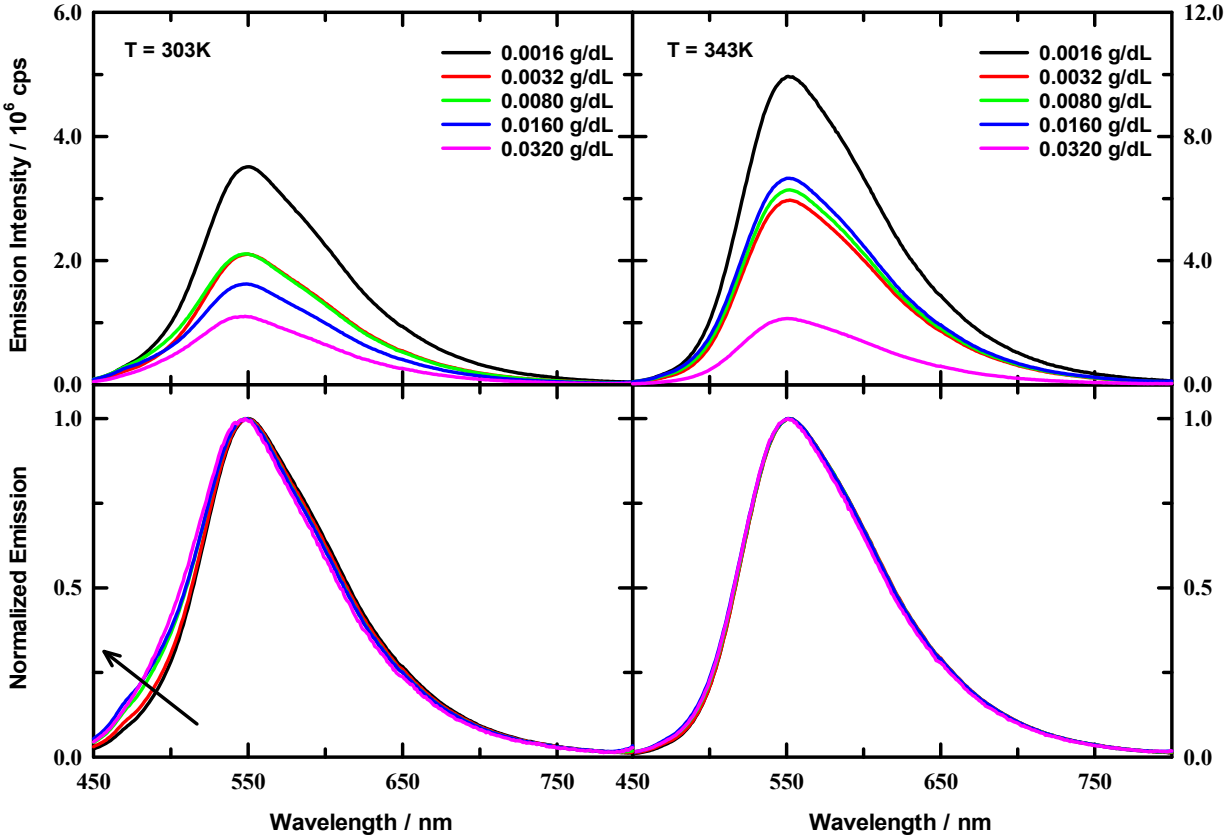


Figure 1. C153 emission spectra for aqueous xanthan gum solutions at various concentrations, as indicated in the legends, and for temperatures at 303 K (**left panels**) and 343 K (**right panels**). Representative spectra are presented in the upper panels for corrected fluorescence intensities and in the lower panels for normalized steady-state emission. The arrow in the lower left panel indicates the spectral response as XG concentration is increased.

To fully characterize the spectra, the concentration dependence is quantified in Figure 2 for absorption (data above the axis break, ~24,000 cm^{-1}) and emission (data below the axis break, ~17,500 cm^{-1}) at each of the temperatures measured here.

The absorption response shows that at 293 K, XG concentration has a negligible effect to within uncertainty (~100 cm^{-1}), until the [XG] = 0.032 g/dL. Upon reaching a sufficiently high XG concentration, there is a substantial blueshift in the C153 absorption that is consistent with C153 more directly interacting with hydrophobic domains within the XG solution structure. The solid blue line is a linear regression applied to the entire data set and is included primarily to emphasize the nonlinear shift in absorption peak frequencies. In their descriptions of linear solvation theory, Lippert [71] and Mataga [72] both predict that the shift in spectral frequency should change linearly as a function of the solvent reaction field, Δf

$$\Delta f = \left(\frac{\varepsilon - 1}{2\varepsilon + 1} - \frac{n_D^2 - 1}{2n_D^2 + 1} \right), \quad (1)$$

which functionally depends on the medium dielectric constant (ε) and index of refraction (n_D), provided that these parameters also change in a linear manner. For frequency shifts that deviate nonlinearly, there must be other solution mechanisms that account for the observed shift. Consistent with other XG literature reports that used spectroscopy, our observed absorption responses suggest changes in the XG conformation [73]. Fluorescence from pyrene showed evidence of concentration-dependent hydrophobicity changes resulting from the acetyl group interactions, which help maintain the XG helical conformation [73]. NMR results also confirm the same observation [26]. We note the same

general pattern in spectral shift at each of the temperatures tested here, from 293 K to 353 K. As a general comment, increasing the temperature at a given XG concentration resulted in a lower C153 energy, discussed in more detail below. The absorption full width at half maximum (FWHM, Figure 2 lower panel) mirrors the concentration-dependent frequency changes, where [XG] = 0.0016 g/dL produces a broad spectrum that narrows with increasing XG concentration, up to [XG] = 0.0160 g/dL. Increasing temperature also produced a narrower absorption spectrum, and C153 reports the formation of a more homogeneous solution. From these absorption results, we see that, upon transition to the excited state, the enhanced C153 dipole moment is sensitive to the local changes driven by XG concentration variation.

Briefly, the emission response seen in Figure 2 is generally similar to absorption with a few noted differences. First, the emission frequencies consistently redshift at all concentrations and are better described by a linear response. Second, while temperature lowers the C153 energy at each concentration, the concentration-dependent peak position becomes negligible at higher temperatures. The two dashed lines in Figure 2 indicate the different concentration-dependent slopes as the temperature increases. However, the redshift between [XG] = 0.0016 g/dL and [XG] = 0.0080 g/dL shows a steeper change compared to [XG] $\geq$ 0.0080 g/dL. If we assume that a linear response should follow from the three most dilute XG concentrations, then the higher concentration emission frequencies deviate negatively from expected values. This suggests that the XG microenvironment at greater XG concentrations either stabilizes the C153 excited state or raises the ground state energy, either of which lowers the transition energy. We have not varied excitation energy here, so at this juncture we cannot differentiate these effects. Nonetheless, the observed emission response shows that the most significant solution changes occur at [XG]~0.0080 g/dL and higher. Emission FWHM data indicate only a small overall change as indicated by the smaller slope of the red regression line compared to the blue absorbance regression line (Figure 2, lower panel).

There are at least two possible scenarios for this observation that may be considered. First, as [XG] increases C153/XG interactions diminish because of stronger and/or more extensive XG-XG interactions that drive intra- and intermolecular associations. A measure of the XG chain associations is given by the overlap concentration, C^*, the polymer concentration at which chain entanglements begin to alter the solution behavior [26,74,75]. In this concentration regime, the solution is considered to transition from a dilute to a semi-dilute system. For XG in water, C^* has been reported to be ~0.02 g/dL [76]. Below this value, XG is in a dilute solution where entanglements between separate chains should be minimized. Takamasa and coworkers cited conformational change between coil and helix along with motional restriction in deacylated XG as their explanation for the NMR line broadening at 288 K [77]. In the same report, they identified the coil-to-helix transition using differential scanning calorimetry. Brunchi and coworkers also used high-resolution NMR to study the interactions of acetate and pyruvate groups, which are known to influence XG chain conformation, and reported that, in 0.0021 g/dL XG solution at 298 K, XG is in the ordered conformation [26]. Consistent with these reports, in dilute XG solution, the C153 spectral response seems to indicate it is better shielded from water interactions compared to more concentrated XG solutions. If one assumes a helical XG conformation at low [XG] and lower temperature [31,78], and if C153 is strongly associated with this motif, then on average it apparently senses a less water-like environment, or at least an environment that is on average less polar. A second possibility might be gleaned by considering an XG organization that may allow for water pool formation within XG nanocages. In such an example, C153 intensity is quenched because of C153/water interactions. As [XG] increases, the decreased emission intensity combined with redshifted emission energy argues that C153 is becoming water-exposed. If local water domains are forming or C153 is expelled away from XG, either possibility would show the observed behavior. The transformation from helix to coil conformation may be complicit in these spectral changes. The most probable

interpretation here is a combination of these, and likely other, interaction effects assuming a randomized distribution of C153 in the bulk solution. What then of temperature effects?

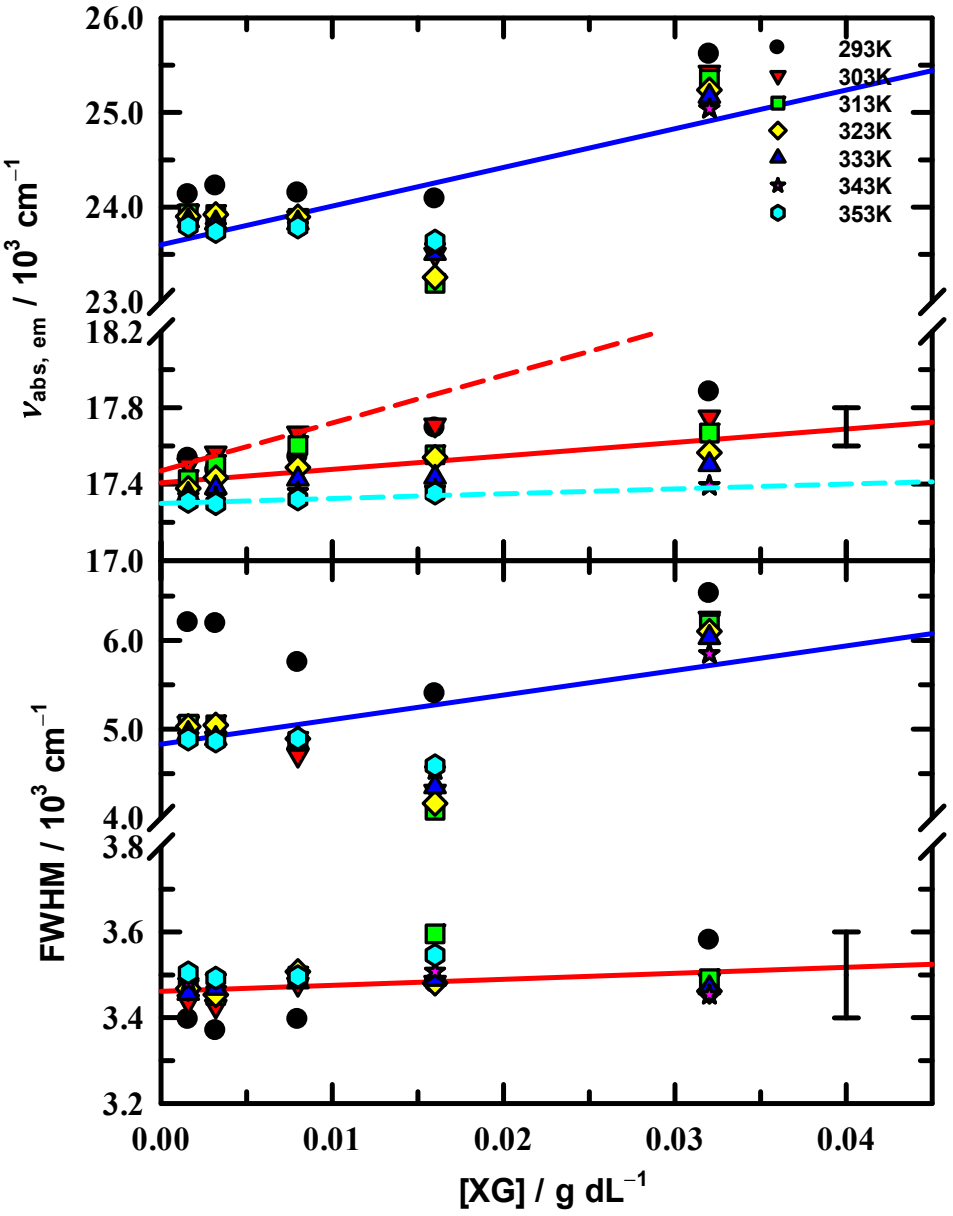


Figure 2. Concentration dependence of the C153 spectral parameters. The upper panel presents first-moment absorption and emission energies computed using intensity-weighted frequencies. The lower panel shows the associated spectral widths, calculated using the full width at half maximum intensity values. A typical error bar ($\pm$100 cm^{-1}) is shown for data below the y-axis break in each panel and is the same magnitude for absorption and emission data. Error bars for data above each axis break are also $\pm$100 cm^{-1} and omitted here because they are the same size as the data points. Solid blue lines are linear regressions to the entire absorbance data set, and red lines to the emission data sets, included only as an aid to assess parameter variations. The dashed red line is a linear regression using only [XG] = 0.0016 g/dL to 0.0080 g/dL at 303 K, and the dashed cyan line is the same data but at 353 K.

3.1.2. Temperature Effect

Temperature is an important parameter in investigating the XG aqueous solution. The intrinsic viscosity of XG in a salt-free solution increases with temperature from 298 K to 348 K, indicating a transition from an ordered to a disordered conformation [26]. In

water, the intrinsic viscosity of XG increased by 30% at 323 K compared to 293 K [76]. XG (1.0 wt % at 288 K) in D_2O shows broadening peaks in ^1H NMR spectra, suggesting helix conformation and coil state. Based on the DSC results, the transition temperature from coil to helix is estimated to occur at 305.5 K [77]. The positive peak of the circular dichroism spectrum of XG in pure water decreased at 353 K and recovered when cooled at 313 K, indicating that the double helical conformation of XG was locally reconstructed by renaturation [79]. How then, does the response from an extrinsic probe molecule compare?

Temperature influence on the C153 spectra is readily observed in Figure 3 and the spectral analysis is given in Figure 4. On heating, the fluorescence intensity increases by approximately 4× from 293 K to 343 K at the limits of XG concentration studied here (upper panels). A more extensive spectral shape change was observed at increased [XG] (Figure 3, lower right panel). Figure 4 shows that the absorption peak frequencies vary smoothly, with a small redshift on the order of ~350 cm^{-1}. The notable exception is [XG] = 0.0160 g/dL (yellow diamonds), where the redshift shows a marked minimum at 313 K. Similarly, C153 emission also shows an overall modest redshift of ~300 cm^{-1}, but interestingly there is first a small rise between 293 K and 303 K that is at the edge of our spectral resolution for these experiments. We also note that [XG] = 0.0320 g/dL shows no such rise and redshifts across the entire temperature range. Spectral FWHM data evidence the pronounced temperature effect. For the [XG] = 0.0016 g/dL, the most dilute solution, the absorption spectra at 293 K are collectively the broadest, with a width of ~6300 cm^{-1} that narrows by ~700 cm^{-1} up to [XG] = 0.0160 g/dL. While increasing the temperature to 303 K reduces the spectral width by >1000 cm^{-1}, there is a secondary effect that indicates the formation of a minimum width for each concentration. The observed width minimum is rather weak up to [XG] = 0.0080 g/dL but significant for [XG] = 0.0160 g/dL at 313 K. For T > 313 K, the three lowest XG concentrations, the widths are essentially constant and the [XG] = 0.0160 g/dL width moderates. The temperature dependence provides further evidence that the most significant solution changes occur at [XG] = 0.0160 g/dL and 313 K. Presuming XG assumes a random coil conformation at increased temperatures, the solution should be generally more homogeneous and C153 appears to sense the solution change. This is also supported by the consistent temperature-dependent emission redshift. Our data compare favorably with the literature that suggests conformational changes occur at roughly 313 K, where we observe a significant shift in spectral response [26,80].

3.2. Time-Resolved Fluorescence

Steady-state absorption and emission give a general sense of solution response to concentration and temperature changes, where the measured responses are the ensemble-averaged data. Through the time-resolved intensity decay, we can extract more detailed information from the excited state radiative relaxation. For example, a probe that experiences multiple chemical environments may show multiple excited-state emission lifetimes that are characteristic of how the microenvironment influences the intensity decay kinetics. In this way, the decay kinetics will be more complicated than is modeled by simple mono-exponential decay, i.e., a single lifetime. As mentioned above, C153 emission intensity is quenched in the presence of water, which results from the decrease in fluorescence quantum yield and, therefore, a decrease in the excited-state lifetime. Thus, the determination of lifetime provides us with an additional and direct means of assessing C153's relative exposure to water.

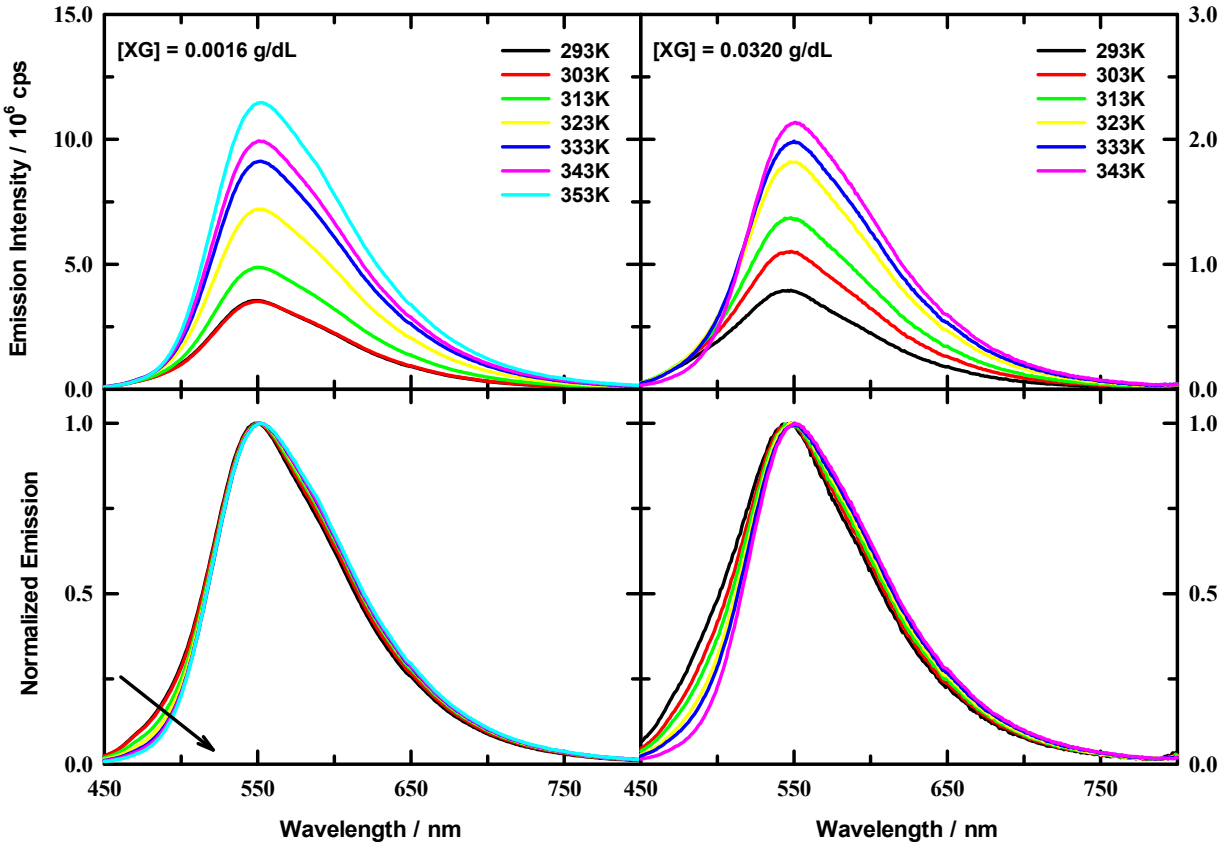


Figure 3. C153 emission spectra for aqueous xanthan gum solutions at various temperatures, as indicated in the legends, and for concentrations at 0.0016 g/dL (**left panels**) and 0.0320 g/dL (**right panels**). Upper panels are for corrected fluorescence intensities and lower panels show normalized steady-state emission. The arrow in the lower left panel indicates the spectral response as temperature increases.

3.2.1. XG Concentration Effect

The intensity decay data were fitted using a simple sum-of-exponentials model and the decay data were best described using two time constants. Reduced chi-squared values were between 1.0 and 1.2 for all fits. Analysis results are presented in Figure 5, showing the lifetime as a function of XG concentration. Whatever the specific XG conformational organization is in water, it should be represented at these most dilute XG concentrations. With that established, we observe C153 lifetimes that indicate no fewer than two distinct solution domains, characterized by a constant lifetime component of 1.7 ns and a second lifetime component of 2.5–4.5 ns that gradually increased with added XG at temperatures less than 333 K. We determined the C153 lifetime in neat water at its emission maximum and found that τ_{flr} = 1.75 ± 0.07 ns. Given this, we can clearly assign the 1.7 ns lifetime value to C153 in a predominantly water environment and, therefore, the longer lifetime must be associated with the C153/XG interactions. Fractional contributions were computed from preexponential decay factors as a simple normalized ratio, $a_i/\Sigma a_i$. We note here as well that a biexponential decay model is the best for all XG concentrations presented here.

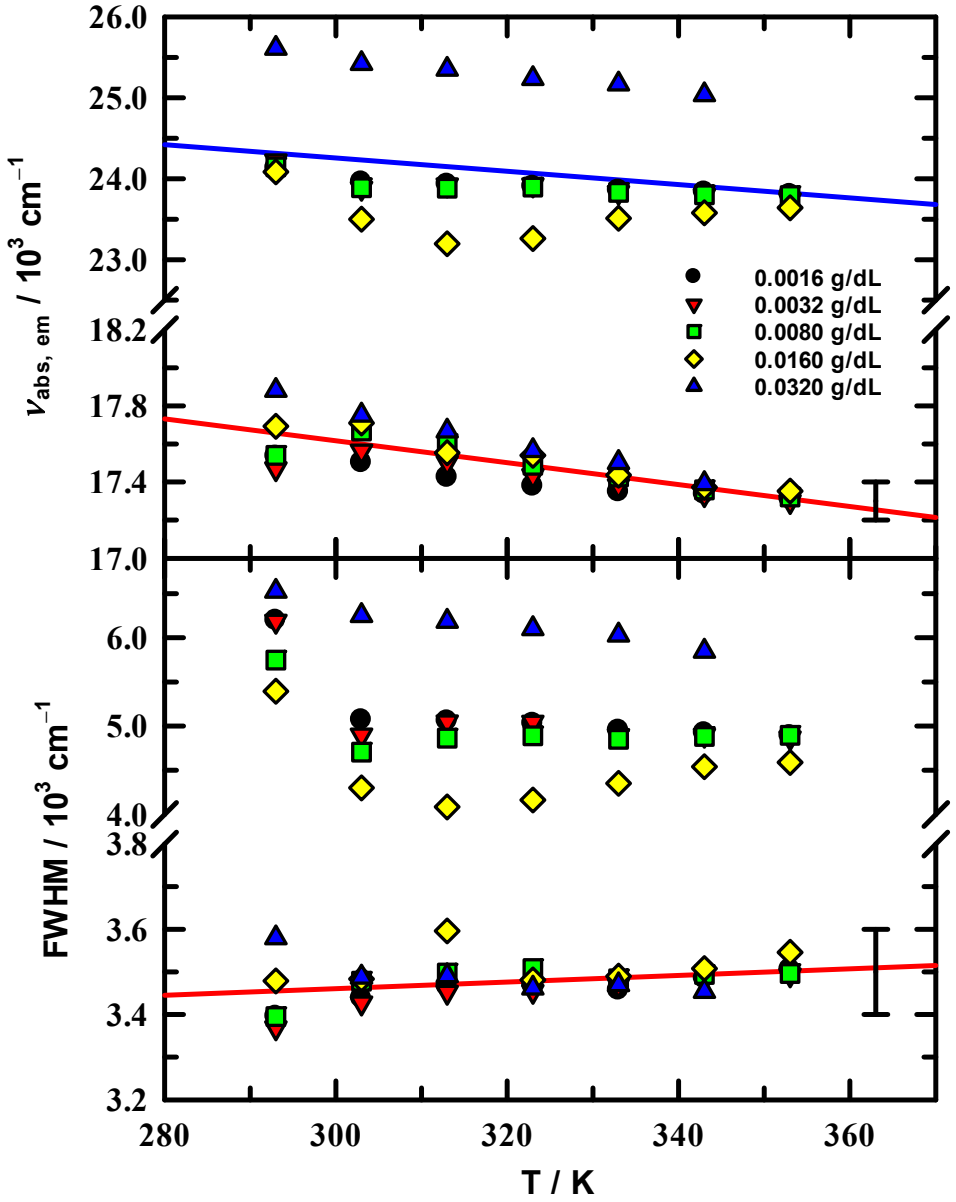


Figure 4. Temperature dependence of the C153 spectral parameters. The upper panel presents first-moment absorption and emission energies computed using intensity-weighted frequencies. The lower panel shows the associated spectral widths, calculated using the full width at half maximum intensity values. A typical error bar ($\pm$100 cm^{-1}) is shown for each parameter and is the same magnitude for absorption and emission data. Error bars for data above each axis break are also $\pm$100 cm^{-1} and omitted here because they are the same size as the data points. Solid blue lines are linear regressions to the entire absorbance data set, and red lines to the emission data sets, included as an aid to assess parameter variations.

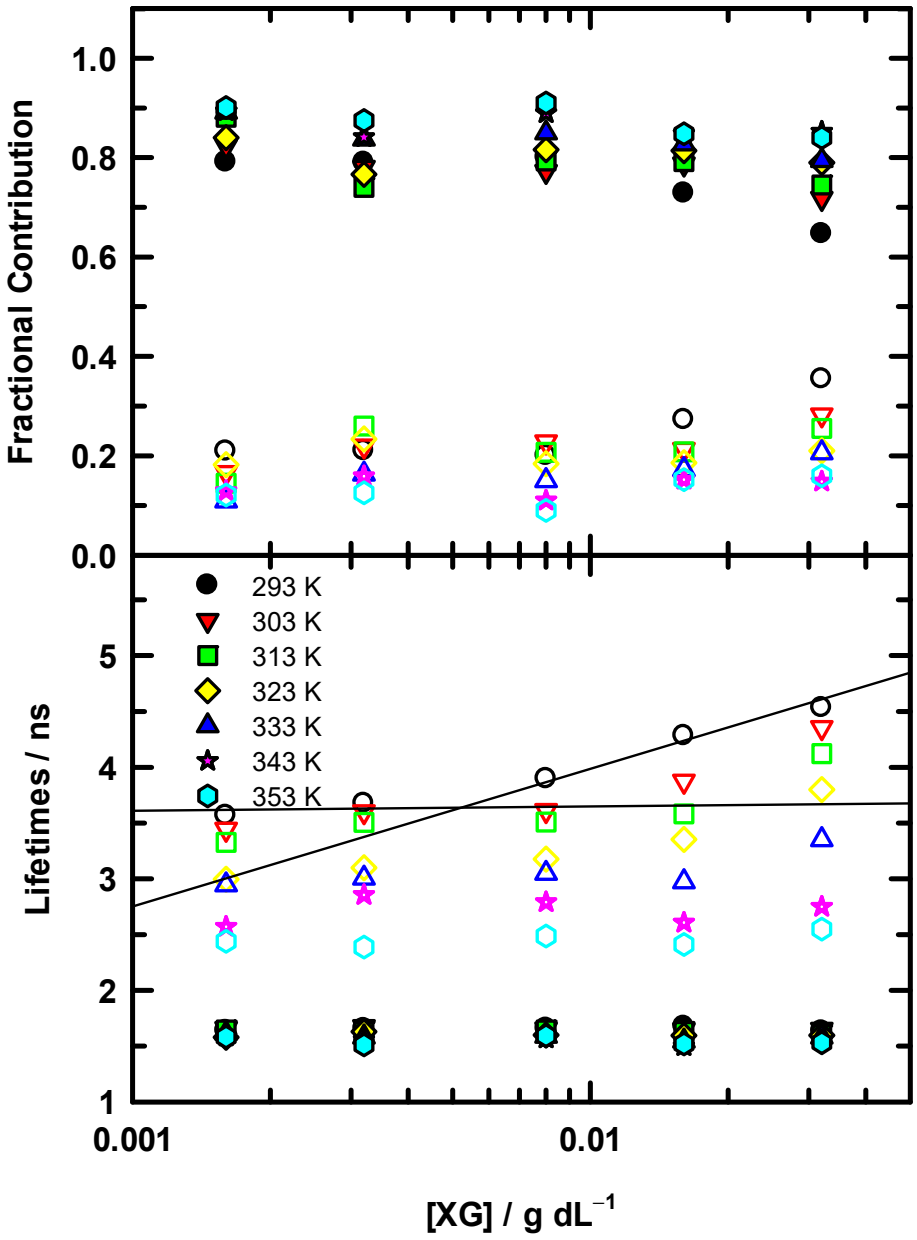


Figure 5. XG concentration dependence of C153 lifetimes and fractional contributions at 293 K. The upper panel shows the fractional contributions for each lifetime component and the lower panel presents the excited-state lifetimes. The solid lines are linear regressions for the longer-lived component at 293 K using two ranges of data, [XG] = 0.00016 to 0.0032 g/dL and [XG] = 0.0080 to 0.0320 g/dL. Error bars are present and contained within the symbol size.

Lifetime contributions at all XG concentrations show that the water component lifetime is the dominant contribution. Importantly, there is a clear break in the linearity for the longer lifetime values (and associated fractional contributions) occurring between [XG] = 0.0032 and 0.0080 g/dL, where the regression lines intersect in Figure 5, mirroring the observations in the steady-state analysis. Below the intersection point, the slope is 0.035 ns dL g^{-1}, and this lifetime variation is less than our measurement uncertainty of ~0.05 ns. The "XG concentrated slope" is 4-fold larger at 1.22 ns dL g^{-1}. It is also important to note that for temperatures above 313 K, the concentration dependence of the lifetime data yields a relatively constant value for the longer time constant that we assigned to C153/XG interactions. The time-resolved data show two distinctly different C153 associations and therefore augment the conclusions reached from the steady-state analysis. Thus, a solidified

picture of solution transition emerges. There is a clear and substantiated transition sensed by C153 in the concentration-dependent changes induced by added XG, the onset of which occurs at [XG]~0.0080 g/dL. Although C^* is larger than this concentration, the C153 molecularity seems to report on what might be considered as a pre-association of XG chain interactions as concentration builds toward the value predicted from bulk viscosity measurements [76].

To thoroughly explore the XG concentration range, we included two additional XG concentrations that are 10-fold and 100-fold diluted from [XG] = 0.0016 g/dL, as reported for the steady-state data, shown in Figure S1. These added concentrations were measured to ensure that we established the decay kinetics approaching XG infinite dilution so that the effects from XG intramolecular interactions were minimized. The constancy of C153 response over at least two orders of magnitude of dilute XG solution maps the concentration range over which there is not likely to be conformational transition(s) or XG-XG associations because the probability of aggregation in dilute solution is small in the concentration range studied here. It appears that what C153 senses is akin to a typical dilute solute/solvent (XG/water) solution. Near to [XG] = 0.01 g/dL, the marked change in C153 lifetime response clearly shows the concentration-dependent onset of XG change. One further point of note is that, along with the two additional diluted XG solutions, we also measured one solution beyond 0.0320 g/dL, at [XG] = 0.0800 g/dL, which was not measured by steady-state emission. Examination of the lifetimes and contributions show that these additional data sets are well aligned with the data patterns of the "main" XG concentrations, which bolsters our confidence in determining a transition point from all of the combined spectroscopic data presented. As one final assessment of the lifetime behavior, we also computed the average lifetime response,

$$\left\langle \tau_{flr} \right\rangle = \sum_i a_i \tau_i, \tag{2}$$

where a_i is the preexponential factor for lifetime τ_i, for what it might reveal about the lifetime landscape. Those data are presented in Figure S2, and we found that they track nearly identically with the shape of the longer lifetime in Figure 5, although shifted to smaller lifetime values because of the constant 1.7 ns contribution.

3.2.2. Temperature Effect

The temperature-dependent lifetimes present an additional perspective and are summarized in Figure 6.

The faster lifetimes show a slight decrease in value, but this is about the same magnitude as the experimental uncertainty, coupled with a corresponding increase in its associated fractional contribution as temperature increases. The contribution approaches ~90% at the highest temperatures for all XG concentrations considered. This is further evidence that C153 becomes more water-exposed as the XG solution structure undergoes transformation by thermal effects. With increased temperature, XG chains become more flexible, and, as mentioned above, XG heating induces a transition to a random coil conformation, as evidenced by the literature reports using SANS, NMR, viscosity, rheometry, and DSC [26,32,64,70,77]. While the shorter lifetime remains essentially constant, the longer lifetime presents a more significant decrease along with a decrease in fractional contribution. Referencing the concentration-dependent data for [XG] < 0.0032 g/dL, we see that the ~4 ns lifetime shortens by ~1 ns. We interpret this to mean that, although there is a significant change to the XG structure, there is likely to be an ensemble effect where C153 still senses XG. It is likely that the solvation environment of the XG structure, both backbone and side chain components, contributes to decreasing the C153 lifetime from 4 ns toward that observed in neat water. Nonetheless, we see a remaining 10% contribution even at the highest temperature studied here.

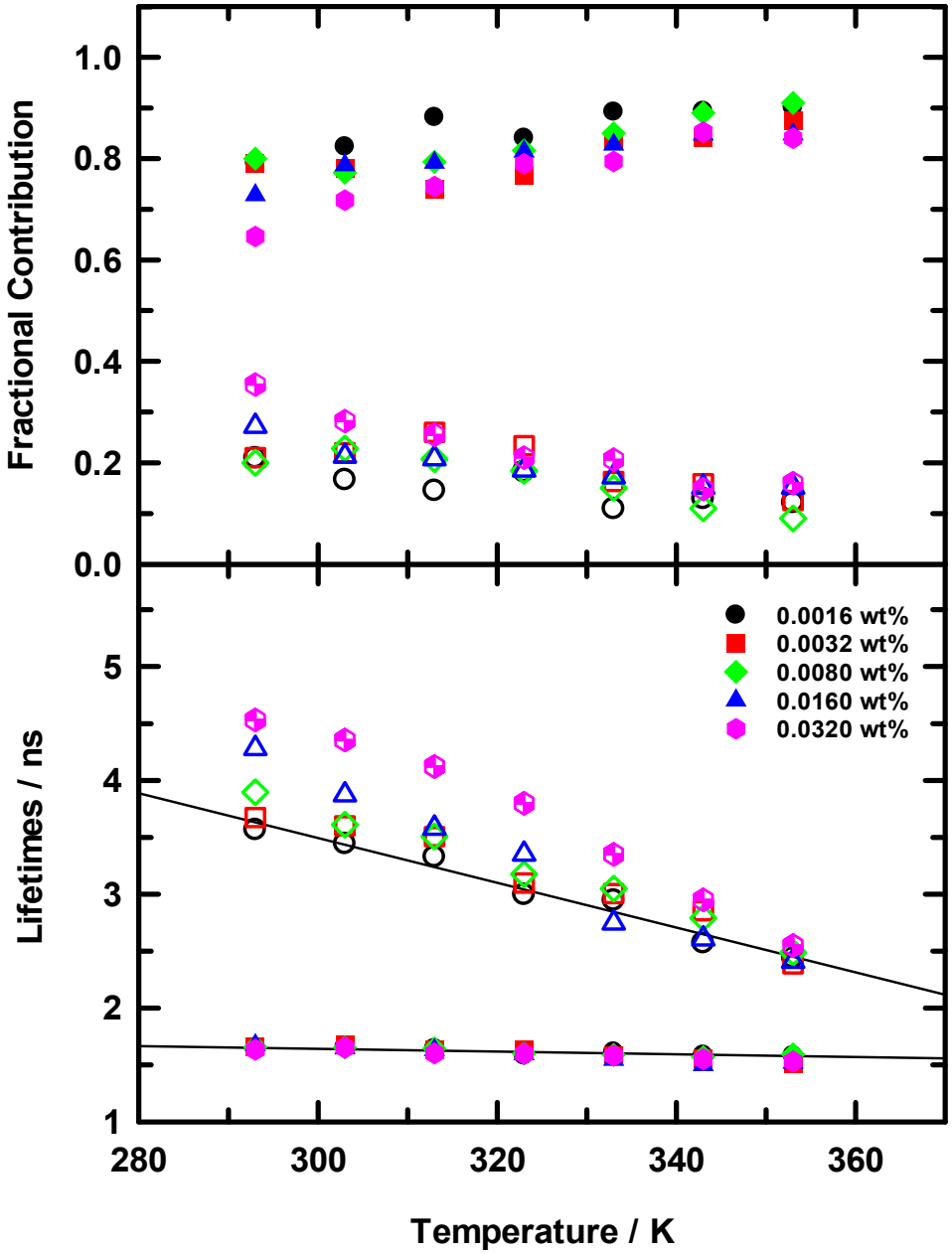


Figure 6. XG temperature dependence of C153 lifetimes and fractional contributions for [XG] = 0.0016 g/dL to 0.0320 g/dL. The upper panel shows the fractional contributions for each lifetime component and the lower panel presents the excited-state lifetimes. In both panels, filled symbols are the parameters that represent the faster lifetime, and open symbols, the longer-lived component. Solid lines show linear regressions for [XG] = 0.0016 g/dL and are present to aid in visualizing the lifetime response. Error bars are contained within the symbol size.

4. Summary and Conclusions

We have demonstrated the utility of fluorescence spectroscopy to provide information on XG solution behavior through the perspective of the sensitive solute molecule, C153. Few reports in the XG literature leverage the advantages and sensitivities offered by fluorescence spectroscopy. The spectroscopic response of a notably sensitive fluorophore, C153, has been used to delineate and quantify the XG concentration and temperature dependence in plain water solutions.

Spectral shifts and widths derived from the C153 ground- and excited-state transition energies support the idea that XG solution heterogeneity becomes significant at

[XG]~0.0080 g/dL. Upon increasing temperature, the local polarity enhancement of the C153 microenvironment by water is evidenced by a spectral redshift. As XG adopts an open, random coil configuration, water more uniformly solvates the XG backbone and side chains, lowering the C153 energy. Spectral widths narrowed and also suggested significant solution changes occurring around [XG] = 0.0080 g/dL. These spectroscopic observations align well with the literature that reports the XG motif transformations between helix and random coil.

The inclusion of intensity decay data can help, to some extent, clarify the emission spectroscopy. Fluorescence lifetimes have resolved two C153 populations of varying percentage contributions. The faster 1.7 ns time constant we assigned to a C153-water microenvironment and a slower time constant at ~3.0 ns associated with C153 interactions within an XG microenvironment. Excited-state fluorescence lifetimes corroborated steady-state observations and clearly showed a distinct transition in the longer of the two time constants at [XG]~0.006 g/dL.

At least three plausible molecular explanations can account for our overall observations. First, C153 is responding to the helix-to-coil transition. If buried in and among XG helices, C153 specifically senses the XG molecular structure. Second, increasing the XG concentration increases the probability of side-chain interactions, thus creating a localized region wherein C153 resides. But, at elevated temperatures the drive by an entropic effect seems to counteract local organization, thus creating a mixed spectroscopic response. A third consideration is the formation of localized water domains by a caging type of XG chain organization. From spectral data alone it is challenging to completely harmonize all of these effects. However, we favor the first possibility given the literature comparisons that apply other instrumental methods such as NMR, SANS, DSC, and viscosity.

Given the complexity of the interactions in this system and the responses we have highlighted here, continued investigations are required to better describe the underlying behavior exhibited by XG in plain water solutions and how it influences spectroscopy. Toward this end, future research efforts aim to use fluorescence polarization to elucidate the dynamic response to varying XG concentration and temperature. The expectation is that the time course of molecular diffusion will help to more clearly differentiate between competing mechanisms such as aggregation vs. conformational change.

Supplementary Materials: The following supporting information can be downloaded at: https://www.mdpi.com/article/10.3390/polysaccharides5040055/s1, Figure S1: XG concentration dependence of C153 lifetimes and fractional contributions; Figure S2: XG concentration dependence of the C153 average lifetimes.

Author Contributions: Conceptualization, M.P.H.; methodology, M.P.H.; formal analysis, E.M.N. and M.P.H.; investigation, E.M.N. and M.P.H.; resources, P.A. and M.P.H.; data curation, E.M.N. and M.P.H.; writing—original draft preparation, E.M.N., P.A. and M.P.H.; writing—review and editing, E.M.N., P.A. and M.P.H.; supervision, M.P.H.; project administration, M.P.H.; funding acquisition, P.A. and M.P.H. All authors have read and agreed to the published version of the manuscript.

Funding: This research was partially funded by the National Science Foundation, grant number 2216375, and the SUNY Brockport Provost Post-tenure Grant Program. E.M.N. was supported in part by the SUNY PRODiG Fellowship program.

Institutional Review Board Statement: Not applicable.

Data Availability Statement: Data may be provided upon request.

Conflicts of Interest: The authors declare no conflicts of interest.

References

1. Petri, D.F.S. Xanthan gum: A versatile biopolymer for biomedical and technological applications. *J. Appl. Polym. Sci.* **2015**, *132*, 42035. [CrossRef]
2. Nsengiyumva, E.M.; Alexandridis, P. Xanthan gum in aqueous solutions: Fundamentals and applications. *Int. J. Biol. Macromol.* **2022**, *216*, 583–604. [CrossRef] [PubMed]

3. Tanwar, M.; Gupta, R.K.; Rani, A. Natural gums and their derivatives based hydrogels: In biomedical, environment, agriculture, and food industry. *Crit. Rev. Biotechnol.* **2024**, *44*, 275–301. [CrossRef] [PubMed]
4. Kumar, P.; Kumar, B.; Gihar, S.; Kumar, D. Review on emerging trends and challenges in the modification of xanthan gum for various applications. *Carbohydr. Res.* **2024**, *538*, 109070. [CrossRef] [PubMed]
5. Kashaudhan, K.; Pande, P.P.; Sharma, J.; Shankar, R.; Nath, A. Modified xanthan gum (natural polymeric material) and its derivative for wastewater treatment: A review. *Environ. Prog. Sustain. Energy* **2024**, e14419. [CrossRef]
6. Zhang, M.; Tian, C.; Ding, J.; Shi, X.; Qiu, L.; Yao, W.; Fan, R. Effective Flotation Separation of Chalcopyrite and Graphite Using Eco-Friendly Xanthan Gum as Depressant. *Miner. Process. Extr. Metall. Rev.* **2023**, *45*, 486–494. [CrossRef]
7. Usman, M.; Taj, M.B.; Carabineiro, S.A.C. Gum-based nanocomposites for the removal of metals and dyes from waste water. *Environ. Sci. Pollut. Res.* **2023**, *30*, 102027–102046. [CrossRef] [PubMed]
8. Jadav, M.; Pooja, D.; Adams, D.J.; Kulhari, H. Advances in Xanthan Gum-Based Systems for the Delivery of Therapeutic Agents. *Pharmaceutics* **2023**, *15*, 402. [CrossRef] [PubMed]
9. Rochefort, W.E.; Middleman, S. Rheology of Xanthan Gum: Salt, Temperature, and Strain Effects in Oscillatory and Steady Shear Experiments. *J. Rheol.* **1987**, *31*, 337–369. [CrossRef]
10. Rezaei, A.; Karami, S.; Karimi, A.M.; Vatanparast, H.; Sadeghnejad, S. New molecular and macroscopic understandings of novel green chemicals based on Xanthan Gum and bio-surfactants for enhanced oil recovery. *Sci. Rep.* **2024**, *14*, 12752. [CrossRef]
11. Zhang, H.; Li, Y.; Fu, Y.; Jiao, H.; Wang, X.; Wang, Q.; Zhou, M.; Yong, Y.-C.; Liu, J. A structure-functionality insight into the bioactivity of microbial polysaccharides toward biomedical applications: A review. *Carbohydr. Polym.* **2024**, *335*, 122078. [CrossRef] [PubMed]
12. Song, Y.; Li, S.; Gong, H.; Yip, R.C.S.; Chen, H. Biopharmaceutical applications of microbial polysaccharides as materials: A Review. *Int. J. Biol. Macromol.* **2023**, *239*, 124259. [CrossRef]
13. Sorze, A.; Valentini, F.; Dorigato, A.; Pegoretti, A. Development of a Xanthan Gum Based Superabsorbent and Water Retaining Composites for Agricultural and Forestry Applications. *Molecules* **2023**, *28*, 1952. [CrossRef] [PubMed]
14. Paudel, A.; Crum, A.N.; Wang, Y. A full metal-free flexible ammonium-ion battery with biodegradable hydrogel electrolyte. *J. Mat. Chem. A* **2024**, *12*, 11975–11985. [CrossRef]
15. Patel, J.; Maji, B.; Moorthy, N.S.H.N.; Maiti, S. Xanthan gum derivatives: Review of synthesis, properties and diverse applications. *RSC Adv.* **2020**, *10*, 27103–27136. [CrossRef] [PubMed]
16. Fu, X.; Qin, F.; Liu, T.; Zhang, X. Enhanced Oil Recovery Performance and Solution Properties of Hydrophobic Associative Xanthan Gum. *Energy Fuels* **2022**, *36*, 181–194. [CrossRef]
17. Morris, E.R. Ordered conformation of xanthan in solutions and "weak gels": Single helix, double helix–or both? *Food Hydrocoll.* **2019**, *86*, 18–25. [CrossRef]
18. Garcia-Ochoa, F.; Santos, V.E.; Casas, J.A.; Gomez, E. Xanthan gum: Production, recovery, and properties. *Biotechnol. Adv.* **2000**, *18*, 549–579. [CrossRef]
19. Holzwarth, G.; Ogletree, J. Pyruvate-free xanthan. *Carbohydr. Res.* **1979**, *76*, 277–280. [CrossRef]
20. de Moura, M.R.V.; Moreno, R. Concentration, Brine Salinity and Temperature effects on Xanthan Gum Solutions Rheology. *Appl. Rheol.* **2019**, *29*, 69–79. [CrossRef]
21. Abu Elella, M.H.; Goda, E.S.; Gab-Allah, M.A.; Hong, S.E.; Pandit, B.; Lee, S.; Gamal, H.; Rehman, A.u.; Yoon, K.R. Xanthan gum-derived materials for applications in environment and eco-friendly materials: A review. *J. Environ. Chem. Eng.* **2021**, *9*, 104702. [CrossRef]
22. Katzbauer, B. Properties and applications of xanthan gum. *Polym. Degrad. Stab.* **1998**, *59*, 81–84. [CrossRef]
23. Reinoso, D.; Martín-Alfonso, M.J.; Luckham, P.F.; Martínez-Boza, F.J. Rheological characterisation of xanthan gum in brine solutions at high temperature. *Carbohydr. Polym.* **2019**, *203*, 103–109. [CrossRef] [PubMed]
24. Milas, M.; Rinaudo, M. Conformational investigation on the bacterial polysaccharide xanthan. *Carbohydr. Res.* **1979**, *76*, 189–196. [CrossRef]
25. Milas, M.; Reed, W.F.; Printz, S. Conformations and flexibility of native and re-natured xanthan in aqueous solutions. *Int. J. Biol. Macromol.* **1996**, *18*, 211–221. [CrossRef]
26. Brunchi, C.-E.; Avadanei, M.; Bercea, M.; Morariu, S. Chain conformation of xanthan in solution as influenced by temperature and salt addition. *J. Mol. Liq.* **2019**, *287*, 111008. [CrossRef]
27. Wyatt, N.B.; Gunther, C.M.; Liberatore, M.W. Increasing viscosity in entangled polyelectrolyte solutions by the addition of salt. *Polymer* **2011**, *52*, 2437–2444. [CrossRef]
28. Wyatt, N.B.; Liberatore, M.W. Rheology and Viscosity Scaling of the Polyelectrolyte Xanthan Gum. *J. Appl. Poly. Sci.* **2009**, *114*, 4076–4084. [CrossRef]
29. Morris, E.R.; Rees, D.A.; Young, G.; Walkinshaw, M.D.; Darke, A. Order-disorder transition for a bacterial polysaccharide in solution. A role for polysaccharide conformation in recognition between Xanthomonas pathogen and its plant host. *J. Mol. Biol.* **1977**, *110*, 1–16. [CrossRef]
30. Sato, T.; Norisuye, T.; Fujita, H. Double-Stranded Helix of Xanthan: Dissociation Behavior in Mixtures of Water and Cadoxen. *Polym. J.* **1985**, *17*, 729–735. [CrossRef]
31. Tomofuji, Y.; Matsuo, K.; Terao, K. Kinetics of denaturation and renaturation processes of double-stranded helical polysaccharide, xanthan in aqueous sodium chloride. *Carbohydr. Polym.* **2022**, *275*, 118681. [CrossRef]

32. Papagiannopoulos, A.; Sotiropoulos, K.; Radulescu, A. Scattering investigation of multiscale organization in aqueous solutions of native xanthan. *Carbohydr. Polym.* **2016**, *153*, 196–202. [CrossRef]
33. Shatwell, K.P.; Sutherland, I.W.; Dea, I.C.M.; Rossmurphy, S.B. The influence of acetyl and pyruvate substituents on the helix-coil transition behavior of xanthan. *Carbohydr. Res.* **1990**, *206*, 87–103. [CrossRef]
34. Rinaudo, M.; Milas, M.; Bresolin, T.; Ganter, J. Physical properties of xanthan, galactomannan and their mixtures in aqueous solutions. *Macromol. Symp.* **1999**, *140*, 115–124. [CrossRef]
35. Philippova, O.E.; Shibaev, A.V.; Muravlev, D.A.; Mityuk, D.Y. Structure and Rheology of Solutions and Gels of Stiff Polyelectrolyte at High Salt Concentration. *Macromolecules* **2016**, *49*, 6031–6040. [CrossRef]
36. Abbaszadeh, A.; Lad, M.; Janin, M.; Morris, G.A.; MacNaughtan, W.; Sworn, G.; Foster, T.J. A novel approach to the determination of the pyruvate and acetate distribution in xanthan. *Food Hydrocoll.* **2015**, *44*, 162–171. [CrossRef]
37. Hungerford, G.; Allison, A.; McLoskey, D.; Kuimova, M.K.; Yahioglu, G.; Suhling, K. Monitoring Sol-to-Gel Transitions via Fluorescence Lifetime Determination Using Viscosity Sensitive Fluorescent Probes. *J. Phys. Chem. B* **2009**, *113*, 12067–12074. [CrossRef] [PubMed]
38. Chauhan, S.; Kaur, M.; Kumar, K.; Chauhan, M.S. Study of the Effect of Electrolyte and Temperature on the Critical Micelle Concentration of Dodecyltrimethylammonium Bromide in Aqueous Medium. *J. Chem. Thermodyn.* **2014**, *78*, 175–181. [CrossRef]
39. Geng, F.; Zheng, L.; Yu, L.; Li, G.; Tung, C. Interaction of Bovine Serum Albumin and Long-Chain Imidazolium Ionic Liquid Measured by Fluorescence Spectra and Surface Tension. *Process Biochem.* **2010**, *45*, 306–311. [CrossRef]
40. Hanczyc, P.; Mikhailovsky, A.; Boyer, D.R.; Sawaya, M.R.; Heeger, A.; Eisenberg, D. Ultrafast Time-Resolved Studies on Fluorescein for Recognition Strands Architecture in Amyloid Fibrils. *J. Phys. Chem. B* **2018**, *122*, 8–18. [CrossRef] [PubMed]
41. Quan, H.; Hu, Y.; Huang, Z.; Wenmeng, D. Preparation and property evaluation of a hydrophobically modified xanthan gum XG-C16. *J. Dispers. Sci. Technol.* **2020**, *41*, 656–666. [CrossRef]
42. Zeng, C.; Zhao, H.; Wan, Z.; Xiao, Q.; Xiaa, H.; Guo, S. Highly biodegradable, thermostable eutectogels prepared by gelation of natural deep eutectic solvents using xanthan gum: Preparation and characterization. *RSC Adv.* **2020**, *10*, 28376–28382. [CrossRef] [PubMed]
43. Shibaev, A.V.; Muravlev, D.A.; Muravleva, A.K.; Matveev, V.V.; Chalykh, A.E.; Philippova, O.E. pH-Dependent Gelation of a Stiff Anionic Polysaccharide in the Presence of Metal Ions. *Polymers* **2020**, *12*, 868. [CrossRef] [PubMed]
44. Krstonošić, V.; Milanović, M.; Dokić, L. Application of different techniques in the determination of xanthan gum-SDS and xanthan gum-Tween 80 interaction. *Food Hydrocoll.* **2019**, *87*, 108–118. [CrossRef]
45. Zdanowicz, M.; Wilpiszewska, K.; Spychaj, T. Deep eutectic solvents for polysaccharides processing. A review. *Carbohydr. Polym.* **2018**, *200*, 361–380. [CrossRef] [PubMed]
46. Kumar, A.; Rao, K.M.; Han, S.S. Application of xanthan gum as polysaccharide in tissue engineering: A review. *Carbohydr. Polym.* **2018**, *180*, 128–144. [CrossRef]
47. Habibi, H.; Khosravi-Darani, K. Effective variables on production and structure of xanthan gum and its food applications: A review. *Biocatal. Agric. Biotechnol.* **2017**, *10*, 130–140. [CrossRef]
48. Lovegrove, A.; Edwards, C.H.; De Noni, I.; Patel, H.; El, S.N.; Grassby, T.; Zielke, C.; Ulmius, M.; Nilsson, L.; Butterworth, P.J.; et al. Role of polysaccharides in food, digestion, and health. *Crit. Rev. Food Sci. Nutr.* **2017**, *57*, 237–253. [CrossRef] [PubMed]
49. Wyatt, N.B.; Liberatore, M.W. The effect of counterion size and valency on the increase in viscosity in polyelectrolyte solutions. *Soft Matter* **2010**, *6*, 3346–3352. [CrossRef]
50. Kimball, J.; Chavez, J.; Ceresa, L.; Kitchner, E.; Nurekeyev, Z.; Doan, H.; Szabelski, M.; Borejdo, J.; Gryczynski, I.; Gryczynski, Z. On the origin and correction for inner filter effects in fluorescence Part I: Primary inner filter effect-the proper approach for sample absorbance correction. *Methods Appl. Fluoresc.* **2020**, *8*, 033002. [CrossRef] [PubMed]
51. Friganović, T.; Weitner, T. Reducing the Inner Filter Effect in Microplates by Increasing Absorbance? Linear Fluorescence in Highly Concentrated Fluorophore Solutions in the Presence of an Added Absorber. *Anal. Chem.* **2023**, *95*, 13036–13045. [CrossRef] [PubMed]
52. Barra, K.M.; Sabatini, R.P.; McAtee, Z.P.; Heitz, M.P. Solvation and Rotation Dynamics in the Trihexyl(tetradecyl)phosphonium Chloride Ionic Liquid/Methanol Cosolvent System. *J. Phys. Chem. B* **2014**, *118*, 12979–12992. [CrossRef] [PubMed]
53. Horng, M.L.; Gardecki, J.A.; Papazyan, A.; Maroncelli, M. Subpicosecond Measurements of Polar Solvation Dynamics: Coumarin 153 Revisited. *J. Phys. Chem.* **1995**, *99*, 17311–17337. [CrossRef]
54. Heitz, M.P.; Sabo, T.J.; Robillard, S.M. Coumarin 153 Dynamics in Ethylammonium Nitrate: The Effects of Dilution with Methanol. *Sustain. Chem.* **2021**, *2*, 778–795. [CrossRef]
55. Moylan, C.R. Molecular hyperpolarizabilities of coumarin dyes. *J. Phys. Chem.* **1994**, *98*, 13513–13516. [CrossRef]
56. Baumann, W.; Nagy, Z. Photoinduced charge transfer as revealed by ground and excited state dipole moments. *Pure Appl. Chem.* **1993**, *65*, 1729–1732. [CrossRef]
57. Reynolds, L.; Gardecki, J.A.; Frankland, S.J.V.; Horng, M.L.; Maroncelli, M. Dipole Solvation in Nondipolar Solvents: Experimental Studies of Reorganization Energies and Solvation Dynamics. *J. Phys. Chem.* **1996**, *100*, 10337–10354. [CrossRef]
58. Cerezo, J.; Gao, S.; Armaroli, N.; Ingrosso, F.; Prampolini, G.; Santoro, F.; Ventura, B.; Pastore, M. Non-Phenomenological Description of the Time-Resolved Emission in Solution with Quantum-Classical Vibronic Approaches-Application to Coumarin C153 in Methanol. *Molecules* **2023**, *28*, 3910. [CrossRef] [PubMed]

59. Królicki, R.; Jarzęba, W.; Mostafavi, M.; Lampre, I. Preferential Solvation of Coumarin 153—The Role of Hydrogen Bonding. *J. Phys. Chem. A* **2002**, *106*, 1708–1713. [CrossRef]
60. Fee, R.S.; Milsom, J.A.; Maroncelli, M. Inhomogeneous Decay Kinetics and Apparent Solvent Relaxation at Low Temperatures. *J. Phys. Chem.* **1991**, *95*, 5170–5181. [CrossRef]
61. Kuznetsova, N.A.; Kaliya, O.L. The photochemistry of coumarins. *Russ. Chem. Rev.* **1992**, *61*, 683–696. [CrossRef]
62. Dobek, K. The Influence of Temperature on Coumarin 153 Fluorescence Kinetics. *J. Fluoresc.* **2011**, *21*, 1547–1557. [CrossRef] [PubMed]
63. Dobek, K.; Karolczak, J. The Influence of Temperature on C153 Steady-State Absorption and Fluorescence Kinetics in Hydrogen Bonding Solvents. *J. Fluoresc.* **2012**, *22*, 1647–1657. [CrossRef] [PubMed]
64. Milas, M.; Rinaudo, M.; Duplessix, R.; Borsali, R.; Lindner, P. Small Angle Neutron Scattering from Polyelectrolyte Solutions: From Disordered to Ordered Xanthan Chain Conformation. *Macromolecules* **1995**, *28*, 3119–3124. [CrossRef]
65. Milas, M.; Rinaudo, M.; Tinland, B. The viscosity dependence on concentration, molecular-weight and shear rate of xanthan solutions. *Polym. Bull.* **1985**, *14*, 157–164. [CrossRef]
66. Banerjee, P.; Mukherjee, I.; Bhattacharya, S.; Datta, S.; Moulik, S.P.; Sarkar, D. Sorption of Water Vapor, Hydration, and Viscosity of Carboxymethylhydroxypropyl Guar, Diutan, and Xanthan Gums, and Their Molecular Association with and without Salts (NaCl, $CaCl_2$, HCOOK, CH_3COONa, $(NH4)_2SO_4$ and $MgSO_4$) in Aqueous Solution. *Langmuir* **2009**, *25*, 11647–11656. [CrossRef] [PubMed]
67. Nsengiyumva, E.M.; Heitz, M.P.; Alexandridis, P. Thermal hysteresis phenomena in aqueous xanthan gum solutions. *Food Hydrocoll.* **2023**, *144*, 108973. [CrossRef]
68. Brunchi, C.-E.; Morariu, S.; Iftime, M.-M.; Stoica, I. Xanthan gum in solution and solid-like state: Effect of temperature and polymer concentration. *J. Mol. Liq.* **2023**, *387*, 122600. [CrossRef]
69. Brunchi, C.E.; Morariu, S.; Bercea, M. Intrinsic viscosity and conformational parameters of xanthan in aqueous solutions: Salt addition effect. *Colloids Surf. B* **2014**, *122*, 512–519. [CrossRef]
70. Papagiannopoulos, A.; Sotiropoulos, K.; Pispas, S. Particle tracking microrheology of the power-law viscoelasticity of xanthan solutions. *Food Hydrocoll.* **2016**, *61*, 201–210. [CrossRef]
71. Lippert, E. Dipolmoment und Elektronenstruktur von angeregten Molekülen. *Z. Naturforschg.* **1955**, *10a*, 541. [CrossRef]
72. Mataga, N.; Kaifu, Y.; Koizumi, M. Solvent Effects upon Fluorescence Spectra and the Dipole Moments of Excited Molecules. *Bull. Chem. Soc. Jpn.* **1956**, *29*, 465–470. [CrossRef]
73. Wang, L.; Xiang, D.; Li, C.; Zhang, W.; Bai, X. Effects of deacetylation on properties and conformation of xanthan gum. *J. Mol. Liq.* **2022**, *345*, 117009. [CrossRef]
74. Brunchi, C.-E.; Morariu, S.; Bercea, M. Impact of ethanol addition on the behaviour of xanthan gum in aqueous media. *Food Hydrocoll.* **2021**, *120*, 106928. [CrossRef]
75. Morris, E.R.; Cutler, A.N.; Ross-Murphy, S.B.; Rees, D.A.; Price, J. Concentration and shear rate dependence of viscosity in random coil polysaccharide solutions. *Carbohydr. Polym.* **1981**, *1*, 5–21. [CrossRef]
76. Nsengiyumva, E.M.; Heitz, M.P.; Alexandridis, P. Salt and Temperature Effects on Xanthan Gum Polysaccharide in Aqueous Solutions. *Int. J. Molec. Sci.* **2024**, *25*, 490. [CrossRef] [PubMed]
77. Takemasa, M.; Nishinari, K. Solution Structure of Molecular Associations Investigated Using NMR for Polysaccharides: Xanthan/Galactomannan Mixtures. *J. Phys. Chem. B* **2016**, *120*, 3027–3037. [CrossRef]
78. Norton, I.T.; Goodall, D.M.; Frangou, S.A.; Morris, E.R.; Rees, D.A. Mechanism and dynamics of conformational ordering in xanthan polysaccharide. *J. Mol. Biol.* **1984**, *175*, 371–394. [CrossRef] [PubMed]
79. Matsuda, Y.; Biyajima, Y.; Sato, T. Thermal denaturation, renaturation, and aggregation of a double-helical polysaccharide xanthan in aqueous solution. *Polym. J.* **2009**, *41*, 526–532. [CrossRef]
80. Brunchi, C.-E.; Bercea, M.; Morariu, S.; Dascalu, M. Some properties of xanthan gum in aqueous solutions: Effect of temperature and pH. *J. Polym. Res.* **2016**, *23*, 123. [CrossRef]

Disclaimer/Publisher's Note: The statements, opinions and data contained in all publications are solely those of the individual author(s) and contributor(s) and not of MDPI and/or the editor(s). MDPI and/or the editor(s) disclaim responsibility for any injury to people or property resulting from any ideas, methods, instructions or products referred to in the content.